Research Article | Vol. 9, No. 8 | 1 Aug 2018 | BIOMEDICAL OPTICS EXPRESS 3731

Biomedical Optics EXPRESS

High-speed, ultrahigh-resolution distal scanning OCT endoscopy at 800 nm for *in vivo* imaging of colon tumorigenesis on murine models

JESSICA MAVADIA-SHUKLA,[1] PAYAM FATHI,[2] WENXUAN LIANG,[1] SHAOGUANG WU,[2] CYNTHIA SEARS,[2] AND XINGDE LI*

[1]*Department of Biomedical Engineering, School of Medicine, Johns Hopkins University, Baltimore, MD 21205, USA*
[2]*Department of Medicine- Infectious Disease, School of Medicine, Johns Hopkins University, Baltimore, MD 21205, USA*
**xingde@jhu.edu*

Abstract: We present the first, most compact, ultrahigh-resolution, high-speed, distal scanning optical coherence tomography (OCT) endoscope operating at 800 nm. Achieving high speed imaging while maintaining an ultrahigh axial resolution is one of the most significant challenges with endoscopic OCT at 800 nm. Maintaining an ultrahigh axial resolution requires preservation of the broad spectral bandwidth of the light source throughout the OCT system. To overcome this critical limitation we implemented a distal scanning endoscope with diffractive optics to minimize loss in spectral throughput. In this paper, we employed a customized miniature 900 µm diameter DC micromotor fitted with a micro reflector to scan the imaging beam. We integrated a customized diffractive microlens into the imaging optics to reduce chromatic focal shift over the broad spectral bandwidth of the Ti:Sapphire laser of an approximately 150 nm 3dB bandwidth, affording a measured axial resolution of 2.4 µm (in air). The imaging capability of this high-speed, ultrahigh-resolution distal scanning endoscope was validated by performing 3D volumetric imaging of mouse colon *in vivo* at 50 frames-per-second (limited only by the A-scan rate of linear CCD array in the spectral-domain OCT system and sampling requirements). The results demonstrated that fine microstructures of colon could be clearly visualized, including the boundary between the absorptive cell layer and colonic mucosa as well the crypt patterns. Furthermore, this endoscope was employed to visualize morphological changes in an enterotoxigenic *Bacteriodes fragilis* (ETBF) induced colon tumor model. We present the results of our feasibility studies and suggest the potential of this system for visualizing time dependent morphological changes associated with tumorigenesis on murine models *in vivo*.

© 2018 Optical Society of America under the terms of the OSA Open Access Publishing Agreement

OCIS codes: (110.4500) Optical coherence tomography; (170.2150) Endoscopic imaging.

References and links

1. G. J. Tearney, S. A. Boppart, B. E. Bouma, M. E. Brezinski, N. J. Weissman, J. F. Southern, and J. G. Fujimoto, "Scanning single-mode fiber optic catheter-endoscope for optical coherence tomography," Opt. Lett. **21**(7), 543–545 (1996).
2. M. J. Gora, M. J. Suter, G. J. Tearney, and X. Li, "Endoscopic optical coherence tomography: technologies and clinical applications [Invited]," Biomed. Opt. Express **8**(5), 2405–2444 (2017).
3. J. M. Poneros, S. Brand, B. E. Bouma, G. J. Tearney, C. C. Compton, and N. S. Nishioka, "Diagnosis of specialized intestinal metaplasia by optical coherence tomography," Gastroenterology **120**(1), 7–12 (2001).
4. I. K. Jang, B. E. Bouma, D. H. Kang, S. J. Park, S. W. Park, K. B. Seung, K. B. Choi, M. Shishkov, K. Schlendorf, E. Pomerantsev, S. L. Houser, H. T. Aretz, and G. J. Tearney, "Visualization of coronary atherosclerotic plaques in patients using optical coherence tomography: comparison with intravascular ultrasound," J. Am. Coll. Cardiol. **39**(4), 604–609 (2002).
5. X. Li, J. Yin, C. Hu, Q. Zhou, K. K. Shung, and Z. Chen, "High-resolution coregistered intravascular imaging with integrated ultrasound and optical coherence tomography probe," Appl. Phys. Lett. **97**(13), 133702 (2010).

#335984 https://doi.org/10.1364/BOE.9.003731
Journal © 2018 Received 25 Jun 2018; accepted 11 Jul 2018; published 17 Jul 2018

Biomedical Optics EXPRESS

6. N. Hanna, D. Saltzman, D. Mukai, Z. Chen, S. Sasse, J. Milliken, S. Guo, W. Jung, H. Colt, and M. Brenner, "Two-dimensional and 3-dimensional optical coherence tomographic imaging of the airway, lung, and pleura," J. Thorac. Cardiovasc. Surg. **129**(3), 615–622 (2005).
7. J. J. Armstrong, M. S. Leigh, D. D. Sampson, J. H. Walsh, D. R. Hillman, and P. R. Eastwood, "Quantitative upper airway imaging with anatomic optical coherence tomography," Am. J. Respir. Crit. Care Med. **173**(2), 226–233 (2006).
8. H. O. Coxson, B. Quiney, D. D. Sin, L. Xing, A. M. McWilliams, J. R. Mayo, and S. Lam, "Airway wall thickness assessed using computed tomography and optical coherence tomography," Am. J. Respir. Crit. Care Med. **177**(11), 1201–1206 (2008).
9. P. R. Herz, Y. Chen, A. D. Aguirre, K. Schneider, P. Hsiung, J. G. Fujimoto, K. Madden, J. Schmitt, J. Goodnow, and C. Petersen, "Micromotor endoscope catheter for in vivo, ultrahigh-resolution optical coherence tomography," Opt. Lett. **29**(19), 2261–2263 (2004).
10. H. L. Fu, Y. Leng, M. J. Cobb, K. Hsu, J. H. Hwang, and X. Li, "Flexible miniature compound lens design for high-resolution optical coherence tomography balloon imaging catheter," J. Biomed. Opt. **13**(6), 060502 (2008).
11. J. Xi, L. Huo, Y. Wu, M. J. Cobb, J. H. Hwang, and X. Li, "High-resolution OCT balloon imaging catheter with astigmatism correction," Opt. Lett. **34**(13), 1943–1945 (2009).
12. D. L. Wang, B. V. Hunter, M. J. Cobb, and X. D. Li, "Super-achromatic rapid scanning microendoscope for ultrahigh-resolution OCT imaging," Ieee J Sel Top Quant **13**(6), 1596–1601 (2007).
13. A. R. Tumlinson, J. K. Barton, B. Povazay, H. Sattman, A. Unterhuber, R. A. Leitgeb, and W. Drexler, "Endoscope-tip interferometer for ultrahigh resolution frequency domain optical coherence tomography in mouse colon," Opt. Express **14**(5), 1878–1887 (2006).
14. A. R. Tumlinson, B. Povazay, L. P. Hariri, J. McNally, A. Unterhuber, B. Hermann, H. Sattmann, W. Drexler, and J. K. Barton, "In vivo ultrahigh-resolution optical coherence tomography of mouse colon with an achromatized endoscope," J. Biomed. Opt. **11**(6), 064003 (2006).
15. W. Yuan, J. Mavadia-Shukla, J. Xi, W. Liang, X. Yu, S. Yu, and X. Li, "Optimal operational conditions for supercontinuum-based ultrahigh-resolution endoscopic OCT imaging," Opt. Lett. **41**(2), 250–253 (2016).
16. J. Xi, A. Zhang, Z. Liu, W. Liang, L. Y. Lin, S. Yu, and X. Li, "Diffractive catheter for ultrahigh-resolution spectral-domain volumetric OCT imaging," Opt. Lett. **39**(7), 2016–2019 (2014).
17. F. Housseau and C. L. Sears, "Enterotoxigenic Bacteroides fragilis (ETBF)-mediated colitis in Min (Apc+/-) mice: a human commensal-based murine model of colon carcinogenesis," Cell Cycle **9**(1), 3–5 (2010).
18. C. L. Sears, A. L. Geis, and F. Housseau, "Bacteroides fragilis subverts mucosal biology: from symbiont to colon carcinogenesis," J. Clin. Invest. **124**(10), 4166–4172 (2014).

1. Introduction

In vitro endoscopic OCT was first demonstrated 20 years ago using a single-mode optical fiber and a gradient-index (GRIN) lens to deliver and collect backscattered light to and from the sample [1]. OCT endoscopes [2] laid the foundation for high-resolution, non-invasive or minimally invasive *in vivo* OCT imaging of internal luminal organs such as the gastrointestinal tract [3], coronary arteries [4, 5], and the respiratory tract [6–8]. Until recently, most endoscopic OCT systems have been implemented at 1300 nm, with the best achievable axial resolution limited to 5-20 µm (in air) [9–11].

Over the past decade there have been several attempts to implement ultrahigh-resolution endoscopic OCT at 800 nm [11–15]. Success has been limited due to the engineering challenges for OCT endoscopes at this wavelength range. Two major challenges are: 1) correcting chromatic aberration in the imaging micro-optics for the broad spectral range and 2) implementing a scanning mechanism for high-speed imaging. Our group recently addressed the first challenge by engineering a diffractive endoscope [15, 16]. In our prior publication, we demonstrated proof-of-concept that off-the-shelf miniature diffractive optics is able to partially compensate chromatic aberration. In this paper we present new customized diffractive optics capable of compensating the chromatic aberration throughout the entire spectral bandwidth of the light source.

Secondly, in the prior publication, circumferential scanning was performed using a capillary tube based homebuilt broadband fiber-optic rotary joint (FORJ). The capillary tube based FORJ had several design and manufacturing challenges, resulting in a limited achievable rotational speed. For example, reliable operation requires that butt-coupled optical fibers within the capillary tube are cleaved perfectly at 90 degrees, which is very challenging to achieve. In addition, high-speed rotation can quickly damage the end surfaces of the two butt-coupled fibers, leading to high loss in throughput. The reliable continuous imaging speed

Biomedical Optics EXPRESS

is often restricted to about 5 frames-per-second. Finally, high efficiency robust FORJs at 800 nm with minimal intensity and spectral modulation and maximal intensity throughput are difficult to design and manufacture, primarily due to the small core size (~4.0 µm) of 800 nm single-mode fiber. Additionally, any optical components used in the FORJs need to be able to handle a broad spectral bandwidth to avoid chromatic aberrations which can otherwise significantly degrade the axial resolution.

To solve these engineering challenges we sought to employ a distal scanning mechanism in lieu of proximal scanning. Distal scanning eliminates the need for an FORJ and readily enables high imaging frame rates (within the range of the micromotor). In this paper, we present for the first time, to the best of our knowledge, the smallest high-speed, ultrahigh-resolution distal scanning endoscope operating at a central wavelength of 800 nm with a compact, 900µm diameter DC micromotor. The DC micromotor is capable of rotating up to 200 revolutions-per-second and was customized to feature only 3 ultrathin wires, each 80 µm in diameter. The customized micromotor also featured a forward-feeding wire configuration which enabled us to minimize the field-of-view blockage down to 7.5% and maintain an overall small form factor (1.78 mm in diameter) for the final endoscope including the protective plastic sheath. The high-speed, ultrahigh-resolution endoscope was demonstrated through *in vivo* imaging in a normal murine colon as well as longitudinal imaging in an APC^{Min} murine colon tumorigenesis model.

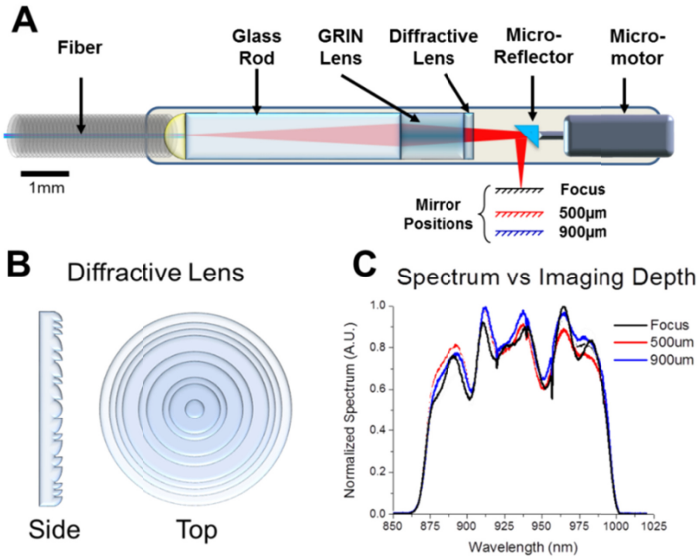

Fig. 1. (A) Schematic of the distal optics design of our distal scanning endoscope. (B) Schematic of the diffractive lens. Side view shows the periodic structure, while the top view showing the concentric ring pattern etched on the element to enable compensation of chromatic aberration. (C) Verification of achromaticity of the imaging optics. The curves are normalized spectra back-reflected from a mirror at the various locations along the imaging depth (i.e. at the focal plane, and 500 µm and 900 µm away from the focal plane as shown in (A)).

2. Methods

2.1 Distal scanning endoscope design

The endoscope design has two key portions, 1) the imaging optics and 2) the beam scanning mechanism. The imaging optics design, shown in Fig. 1(A), is similar to our previous work [16] and is briefly described here. A Corning HI 780 single-mode fiber was used to deliver light from the sample arm of the OCT interferometer to the endoscope optics. The endoscope

Biomedical Optics EXPRESS

optics consisted of a 1 mm diameter glass rod to expand the beam, a 1 mm gradient index (GRIN) lens, and a 1 mm diffractive lens to focus the beam. A desired working distance can be achieved by choosing a proper length of the glass rod and the pitch for the GRIN lens. For example, considering the target beam focus position was ~1.9 mm away from the GRIN lens end surface, the resulting design has a 3.1 mm long glass rod and 0.14 pitch GRIN lens.

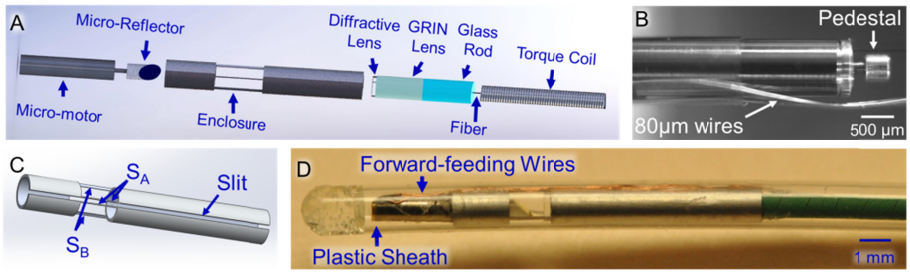

Fig. 2. (A) Detailed distal end schematic of our endoscope. (B) Photograph of the customized 900 μm diameter DC micromotor. (C) 3D drawing of the laser-cut enclosure. S_A: Two ultrathin struts supporting the slit running along the length of the enclosure, S_B: Two remaining struts placed ± 108° from support struts S_A. (D) Photograph of the assembled endoscope inside a protective plastic sheath (of an overall outer diameter of 1.78 mm). An arrow in (D) and an arrow in (B) point to the forward feeding wires which exit the motor proximally and run from the back towards the motor shaft, avoiding wires bending-180° around the motor.

In order to achieve ultrahigh axial resolution imaging throughout the full imaging depth it is necessary to compensate for the chromatic aberration to ensure that the full spectral bandwidth can propagate throughout the system. To prevent any loss of spectral bandwidth in the endoscope optics, we integrated a customized diffractive microlens into the imaging optics. Figure 1(B) illustrates the schematic of the diffractive lens. The side view shows the periodic structure, while the top view shows the concentric ring pattern etched on the microlens. To verify the resulted achromaticity of the imaging optics, we measured the back-reflected spectra from a mirror located at different positions along the imaging depth (including the focal plane, and 500 μm and 900 μm away from the focal plane as seen in Fig. 1(A)) using a broadband, low-power SLD as the input light source. The broadband SLD had a central wavelength of 880 nm and a 10dB spectral bandwidth of 182 nm enabling us to test the chromatic performance of the diffractive compound lens over a broader spectrum than the Ti:Sapphire laser used for the animal model imaging studies. As shown in Fig. 1(C), the normalized back-reflected spectra remain nearly unchanged at various locations away from the focal plane, demonstrating the excellent achromatic performance of the imaging optics. The overall imaging optics achieved a target working distance of ~260 μm (measured from the outer surface of the protective plastic sheath of the endoscope to the focal plane), an axial resolution of 2.4 μm, a lateral resolution of 7.6 μm, and a low round-trip loss of ~2.0 dB.

The mechanical design of the distal scanning endoscope is the second key feature and is shown in Fig. 2(A). The first component is a customized 900 μm diameter DC micromotor (photograph shown in Fig. 2(B)). We chose to employ a miniature DC micromotor due to its robustness, ease of integration and insensitivity to magnetic fields (compared to the AC micromotor by Kinetron Inc.). The micromotor was customized to provide 3 forward feeding wires, each 80 μm in diameter, and a pedestal, 300 μm in diameter, on the motor shaft to facilitate mounting of a miniature reflector. A 500 μm diameter gold-coated rod reflector was used to deflect the beam by ~100° to the sample.

The miniature micromotor was then inserted into a customized enclosure, shown in Fig. 2(C). The customized enclosure was manufactured from 18-gauge extra-thin wall stainless steel hypodermic tubing with an outer diameter (OD) of 1.27 mm and an inner diameter (ID) of 1.1 mm. In order to maintain mechanical and structural integrity while minimizing the field of view blockage, the enclosure was designed with three 1.5 mm long windows separated by

Biomedical Optics EXPRESS

thin struts ~35 µm wide. An important design feature of the enclosure is that it has a small slit, ~160 µm wide, running down the full length of the enclosure as seen in Fig. 2(C). This slit has an ideal width so that the three ultrathin motor drive wires can fit within it, enabling us to safely perform pull-back of the endoscope within the protective plastic sheath. With this design, the total field of view blockage (3 struts and 1 drive-wire-slit) is only 7.5%. A photo of the assembled endoscope is shown in Fig. 2(D) as encased by a transparent protective plastic sheath with an overall OD of 1.78 mm and a total rigid length of 12.5 mm.

2.2 SD-OCT engine

The spectral-domain OCT (SD-OCT) engine used in this paper has been described previously [15, 16]. In brief, as shown in Fig. 3, the SD-OCT engine employs a fiber-optic Michelson interferometer, a broadband light source, and a broadband linear-k-spectrometer. The light source is a home-built, broadband Ti:Sapphire laser with a 3dB bandwidth of 150 nm and a central wavelength of ~825 nm.

The broadband spectrometer is composed of a volumetric diffraction grating with a density of 1,200 line-pairs-per-mm, a multi-element scan lens and a 2,048-pixel linear CCD array. The CCD was able to acquire data at 70,000 A-lines-per-second with 12-bit resolution. The overall spectrometer design achieved a measured signal fall-off of −16 dB over the calibrated imaging depth of 1.23 mm.

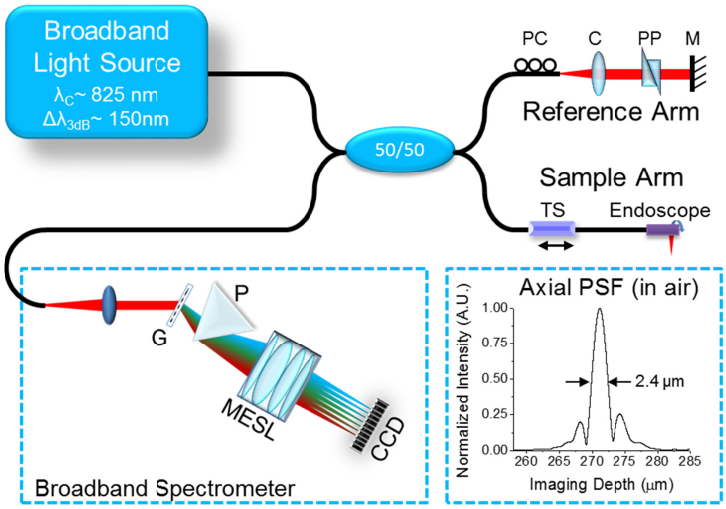

Fig. 3. Ultrahigh-resolution endoscopic SD-OCT system. Linear-k-spectrometer: G: volumetric transmission grating, P: prism, MESL: multi-element scan lens. Reference arm: PC: polarization controller, C: collimator, PP: prism pair, M: mirror. Sample arm: TS: linear translation stage. Inset: representative axial point spread function from the ultrahigh-resolution OCT endoscope.

2.3 Experimental procedure

To demonstrate the performance of the endoscope we imaged the colon of a 3-week-old adult APC^{Min} mouse *in vivo* under a protocol approved by the Animal Care and Use Committee at the Johns Hopkins University. Intraperitoneal injections of 100 mg/kg Ketamine and 10 mg/kg Xyalzine were used to induce and maintain anesthesia during imaging. Prior to imaging, the protective plastic sheath of the OCT endoscope was marked every centimeter from the tip of the endoscope to a distance 4 centimeters away. The endoscope was then directly inserted into the rectum no greater than 4 centimeters followed by volumetric OCT imaging through pullback. A maximum insertion length of 4 centimeters was used to decrease the likelihood of colon perforation.

Biomedical Optics EXPRESS

2.4 Imaging parameters

In order to achieve high-speed imaging without sacrificing image quality, each OCT image frame consisted of 1,397 A-lines, resulting in a ~5.2 µm pixel size in the circumferential direction. With an A-scan rate of ~70,000 A-lines-per-second the frame rate was 50 frames-per-second. The imaging frame rate was governed by the A-line sampling density and was ultimately limited by the A-scan rate of the linear CCD array in the spectrometer. Further reduction in the number of A-lines per frame would reduce image quality and the ability to visualize key attributes of colon such as colonic crypts. Additionally, for the customized micromotor employed in this endoscope running at 50 frames-per-second, we did not observe any non-uniform rotational distortions (NURD) and no NURD related processing as applied to the cross-sectional OCT images.

In order to obtain a full volumetric scan of the mouse colon, pullback was performed with a motorized translation stage. A pitch of 20 µm was maintained between adjacent image frames for a total length of ~30 mm. The entire volumetric scan, consisting of 1,500 circumferential B-frames, was collected within approximately 30 seconds.

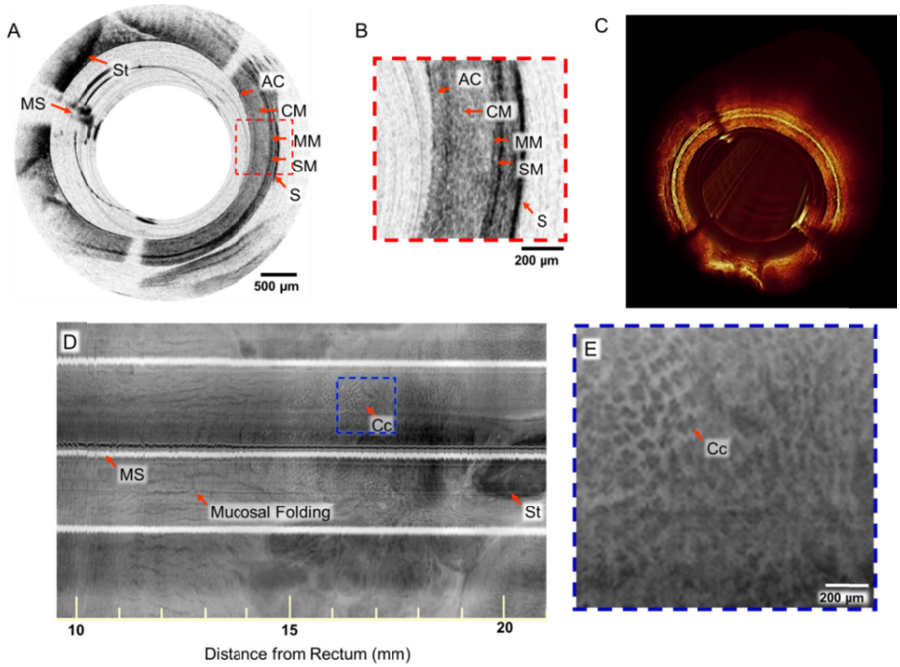

Fig. 4. (A) Representative cross-sectional image of mouse colon *in vivo* and (B) 3x zoomed view of the region indicated by the red dashed-line box on the cross-sectional image in (A), showing boundary between absorptive cell layer and colonic mucosa. AC: absorptive cell lining, CM: colonic mucosa, MM: Muscular mucosa, SM: submucosa, S: serosa, MS: metal strut, St: stool. (C) Volume rendering of an about 11.5 mm long segment of one representative 3D pullback scan. (D) Flattened *en face* intensity projection view of a representative portion of the colon during pullback imaging and (E) 5x zoomed view of the region marked by the blue dashed-line box in (D), highlighting crypt structure of colon. MS: metal strut, Cc: colonic crypts.

3. Results

3.1 In vivo murine colon imaging

Figure 4(A) shows a representative cross-sectional image of control (normal) mouse colon *in vivo*, where normal structures such as the absorptive cell layer, colonic mucosa, muscular mucosa, submucosa, and serosa are visible. To clearly visualize the delicate boundary

Biomedical Optics EXPRESS

between the absorptive cell layer and the colonic mucosa, the region marked by a red dashed-line box was digitally magnified 3x and shown in Fig. 4(B), where structures are more clearly visible.

To further visualize the entire 3D pullback scan at once, we can look at Fig. 4(C) which is a volume rendering of an approximately 11.5 mm long segment of one representative pullback scan and Fig. 4(D) the flattened, depth averaged *en face* intensity projection view. The scale bar in Fig. 4(D) denotes the pullback distance of the OCT endoscope within the colon. Signal void regions (i.e., the 3 white horizontal stripes) are the portions of the image that were blocked by the struts of the metal enclosure. In this *en face* view, we can visualize the intestinal crypt patterns of the colon, mucosal folding as well as stool which is marked by a hyper-intense region around 20 mm pullback distance. Finally, Fig. 4(E) illustrates a 5x zoomed-in region marked by a blue dashed-line box in Fig. 4(D). The zoomed-in region highlights the intestinal crypt pattern which could potentially be clinically relevant to study morphological changes in colonic mucosa in diseases such as colon cancer.

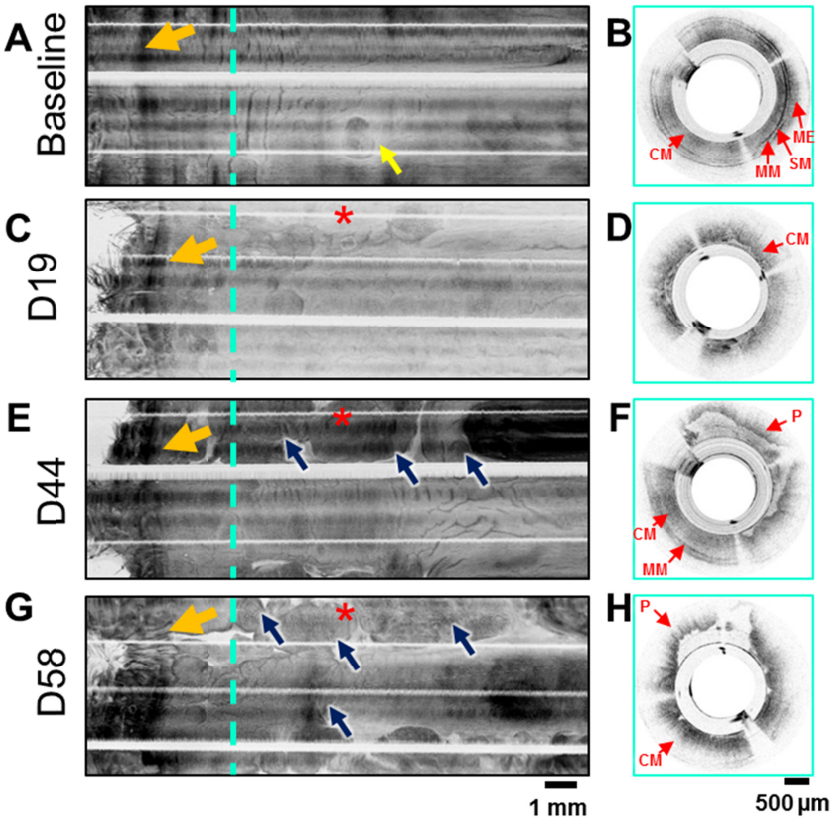

Fig. 5. *En face* intensity projection views and cross-sectional views of mouse colon. The progression from mainly uniform and homogenous baseline structural image (A) to many abnormal looking polyp structures clearly visible (C), (E), (G) as the disease progresses to day 58. The orange arrows point to the transition from colon to rectum marked by the sudden hyperintense signal region. The dark blue arrows point to abnormal regions corresponding to suspected tumors and the red asterisks indicate the location of a growing tumor. The red asterisks lie above a region which has rapidly develop a tumor. Cross-sectional images (B), (D), (F) and (H) are from a representative location in (A), (C), (E), and (G) indicated by the cyan dashed line. Several structures are labeled on the cross-sectional images. CM: colonic mucosa, MM: muscularis mucosa, SM: submucosa, ME: muscularis externa, and P: polyp.

Biomedical Optics EXPRESS

3.2 Feasibility of longitudinal imaging of enterotoxigenic Bacteriodes fragilis (ETBF) induced murine colon tumorigenesis

After confirming the ability to perform ultrahigh-resolution and high-speed endoscopic imaging of mouse colon *in vivo*, we performed longitudinal imaging in a bacteria induced murine colon tumorigenesis model. In these experiments, APC^{Min} mice were infected with enterotoxigenic *Bacteriodes fragilis* (ETBF). ETBF induced colon tumorigenesis in APC^{Min} mice is a model for human commensal colorectal cancer (CRC) that can be used to study morphological changes leading up to cancer. APC^{Min} mice have a mutation in one allele of the *apc* gene resulting in spontaneous small bowel tumor formation. In this model, after ETBF colonization, mice experience severe colitis and shedding of the intestinal epithelial lining for approximately 2 weeks, after which distal colon tumors form and grow rapidly over time [17, 18].

In order to test the ability of this ultrahigh-resolution, high-speed, endoscopic OCT system to monitor longitudinal changes in the colon, we imaged the mice at 8 time points. Initial baseline imaging was performed on the animals before being infected with ETBF. No imaging was performed during the 2 weeks following the infection, to allow ETBF to successfully colonize in the colon and allow recovery from colitis. The first imaging time point after the initial baseline imaging was set to approximately 2 weeks (or until mice recovered from acute colitis).

Figure 5 shows the *en face* depth averaged intensity projection view of a volumetric scan from each time point during longitudinal imaging. Figure 5(A) is the baseline image and Fig. 5G shows the last time point before the animal was sacrificed.

In addition to the *en face* projection views, a cross-sectional OCT image from a representative location marked by the cyan dashed line (in each image) is shown to the right in Figs. 5(B), 5(D), 5(F) and 5(H). The cross-sectional images clearly reveal the changing morphology of the colon during ETBF-induced carcinogenesis. The baseline image, Fig. 5(B), shows normal colon structures such as the colonic mucosa, muscularis mucosa, submucosa, and muscularis externa. By day 19 (Fig. 5(D)) the colonic mucosa has high signal attenuation due to continued inflammation (from colitis). Figure 5(F) shows an image from day 44 where inflammation appears to have subsided, yielding normal looking structures around the 7 o'clock location and high signal attenuation near the 1-2 o'clock and 5 o'clock locations. The high signal attenuation is most likely due to the presence of a polyp. Finally, by time point day 58, the image in Fig. 5(H) shows relatively high signal attenuation across the whole image frame with a suspected polyp at the 11 o'clock region. Similarly, in the *en face* projection views (Figs. 5(A), 5(C), 5(E), and 5(G)), the dark blue arrows point to abnormal regions corresponding to suspected tumors. Furthermore, the red asterisks in each *en face* is overlaid on a tumor that could be seen growing as time progressed from day 19 to day 58. These imaging results demonstrate the capability of the ultrahigh-resolution, high-speed endoscope for visualizing morphological changes longitudinally during cancer development.

4. Discussion and conclusion

High-speed, ultrahigh-resolution endoscopic imaging with a distal scanning probe at 800 nm was demonstrated in this paper. By employing a compact (900 μm) micromotor, we were able to eliminate the need for challenging components such as an FORJ, increase the overall imaging frame-rate, and maintain an overall small foot print for the endoscope. We were able to perform *in vivo* imaging at 50 frames-per-second, limited only by the line-scan rate of the linear CCD array in the spectrometer. By upgrading the linear CCD to a higher speed linear CMOS array in the future, we will be able to effectively double the imaging frame rate.

The ultrahigh axial resolution of 2.4 μm (in air) was achieved by integrating a customized diffractive microlens into the distal end optics of the endoscope. The achromatic performance of the customized diffractive microlens was verified by the nearly invariant normalized back-

Biomedical Optics EXPRESS

reflected broad spectra measured along the imaging depth, demonstrating a minimal chromatic focal shift.

Finally, we demonstrated that the distal scanning endoscope was capable of high-speed, ultrahigh-resolution endoscopic imaging of small lumens (such as mouse colon) *in vivo*. Distal scanning afforded us several advantages including speed, enhanced scanning stability and thus improved imaging quality. These features were demonstrated by the results of *in vivo* murine colon imaging and visualization of delicate microstructures such as the boundary of the absorptive cells and colonic mucosa (Fig. 4(B)) and crypt patterns specific to the gastrointestinal tract (Figs. 4(D) and 4(E)). Furthermore, we demonstrated the feasibility of using the ultrahigh-resolution endoscope for longitudinally studying the morphological changes *in vivo* in an ETBF-induced colon tumorigenesis model. This study demonstrated the robust mechanical design and capability of the endoscopic probe to provide high quality images of time-dependent changes during tumorigenesis. Future systematic studies will be needed to correlate morphological changes visualized in the OCT images with histology at each individual time point. To conclude, it is expected that, as the frame rate continues to be improved and the micromotor cost continues to decrease, the high-speed, ultrahigh-resolution distal-scanning endoscopic imaging system at 800 nm with improved imaging resolution and contrast can potentially benefit various translational applications by offering a better assessment of morphological changes.

Funding

National Institutes of Health (R01CA153023 and R01HL121788); The Wallace H. Coulter Foundation.

Acknowledgments

The authors would like to thank Jiefeng Xi, Hyeon-Cheol Park, and Wu Yuan for their helpful discussions. We would also like to acknowledge the participation of Namiki Precision of California in providing us with customized micromotors.

Disclosures

The authors declare that there are no conflicts of interest related to this article.